

High-Performance transparent Meta-surface for C-/X-Band Lens Antenna Application

Tong Cai¹, Guangming Wang

Air and Missile Defend College, Air force Engineering University, Xi' an 710051, China.

E-mail: caitong326@sina.cn

Abstract. A novel strategy of designing high-performance transparent meta-surfaces is proposed by using an ABBA system. The ABBA element provides a new freedom to largely enhance the transmission of a transmissive meta-surface and suppress the fluctuations in the transmission amplitude by tuning the coupling among cascaded layers. Dual-band operating property is straightforwardly performed by employing the polarization-control principle. A well-designed transparent meta-surface, operating at $f_1=6.5$ GHz and $f_2=10.5$ GHz, consists of 13×17 ABBA elements with parabolic phase distributions along different dimensions. Perfect focusing effects with the same focal length and small reflection are unambiguously observed at both frequencies under excitation of differently-polarized waves, indicating strong phase compensating capacities and high efficiencies of the meta-lens. For practical application, a dual-band lens antenna (LA) is implemented by launching the carefully-designed meta-lens with a self-made Vivaldi antenna. Numerical and experimental results coincide well, indicating that the proposed LA advances in many aspects such as high radiation gain of 18.7 dB at f_1 and 23 dB at f_2 , competitive aperture efficiencies better than 30% and also a simple fabrication process based on a standard printed-circuit-board (PCB) technology. The finding opens up a new avenue to design high-performance meta-surfaces operating in multi-band or achieving integrated functionalities.

1. Introduction

Electromagnetic (EM) control plays an essential role in both science and technology, and has become a research spot with remarkable achievements. Recently, gradient meta-surfaces (GMSs) [1], proposed by YU et al, have provided a powerful solution to solve the mentioned issues due to their strong abilities to manipulate the reflections or refractions of incoming waves by locally controlling the phase and amplitude of the designed meta-atoms within a deep-subwavelength scale. As a result, different kinds of EM manipulation and a lot of fascinating phenomena have been discovered, including wavefront control (the generalized law of refraction/reflection [1], meta-holograms [2], polarization beam splitter [3], focusing [4]), functionality extension (multi-functional device design: bi-functional lens [5], bi-functional devices achieving focusing and vertex effects), polarization control (quarter-wave plate, polarizer) and also multi-frequency system realization [6-7]. Multi-band operating devices have attracted increasing attention for their capability of improving the communication quality, achieving EM integration and reducing device costs. Several techniques, controlling the EM responses by optimized meta-surfaces, have been reported very recently to realize multi-frequency operating devices [6]-[7]. Firstly, a straightforward method of achieving multi-band devices is to use several electric or magnetic resonators with different dimensions, and some relevant absorbers are designed



and experimentally demonstrated [6]. Secondly, multi-mode resonators have been intensively investigated to realize multi-band devices [7]. However, the mentioned methods suffer from mutual coupling and sensitivity of the working frequencies. Especially, these techniques face huge challenges to design multi-band GMSs since it is uneasy to realize a complete phase-shift range over 360° at several separate frequencies without mutual interactions. For the multi-band reflective GMSs, multi-layer structures are independently controlled and optimized, which requires a large frequency interval and becomes invalid for a small frequency interval [8]. Transparent GMSs design is quite challenging for not only requiring a complete phase-shift range over 360° but also needing high transmission amplitude [9]. Therefore, conventional transparent GMSs is limited with low-efficiency, single operating frequency and complex configurations. To the best of our knowledge, high-efficiency transparent GMSs incorporating dual-band operating property, in addition to perfect focusing effects, are rarely studied in the open literature.

In this paper, we propose a new ABBA system to enhance the transmission efficiency of a transparent meta-surface. Compared with the conventional cascaded element (AAAA element), the proposed one increases another design freedom to modulate the coupling among different layers and to suppress the fluctuations in the transmission amplitude. Moreover, inspired by the method of manipulating the transmission beams through polarizations in our work [9], here, we control the operating frequencies of a transparent meta-surface through two orthogonal polarizations. For experimental demonstration, we conceived and realized a high-efficiency transparent meta-surface using the ABBA elements to realize a focusing lens operating in C and X bands with the same focal length. Finally, by carefully launching the lens with a wideband Vivaldi antenna at the focal point, we numerically and experimentally designed and optimized a dual-band lens antenna (LA).

2. Working mechanism of dual-band meta-surface and ABBA element design

We will provide a general strategy to achieve dual-band operating property and high-efficiency transmission of a transparent meta-surface, respectively. For an anisotropic element with mirror symmetries located at (x, y) , the EM response can be described by the matrices \mathbf{R} and \mathbf{T} , where

$$\mathbf{R}(x, y) = \begin{pmatrix} r_{xx, f_1}(x, y) & 0 \\ 0 & r_{yy, f_2}(x, y) \end{pmatrix} \quad (1)$$

$$\mathbf{T}(x, y) = \begin{pmatrix} t_{xx, f_1}(x, y) & 0 \\ 0 & t_{yy, f_2}(x, y) \end{pmatrix} \quad (2)$$

For a perfect transparent element, the reflection coefficient satisfies $\mathbf{R}=0$, while the transmission coefficient satisfies $\mathbf{T}=1$. Here, under the condition of $|t_{xx}|=1$ and $|t_{yy}|=1$, we can control the transmission phases φ_{xx} and φ_{yy} by the local structures, respectively. From the angle of wavefront shaping, three fascinating properties can be found in Fig. 1. In the first case, with a different phase gradient along x and y directions for GMS1 ($\varphi_{xx}=\xi_1 x$, $\varphi_{yy}=\xi_2 x$), differently-polarized waves can split into two beams by passing through the meta-device, which results in an intriguing polarization beam splitter (PBS) [3], [9]. In the second case, referring to Figs. 1(c) and 1(d), beam deflector and focusing lens can be switched freely by illuminating GMS2 ($\varphi_{xx}=\xi x$, $\varphi_{yy}=k_0(\sqrt{F^2+x^2+y^2}-F)$) with differently-polarized waves, which is very interesting to satisfy the requirement of functional integration in the field of photonics. Finally, we can realize operating frequency control conveniently and precisely by modulating the phases in different dimensions of the transparent meta-surface. As shown in Figs. 1(e) and 1(f), with phase distributions of $\varphi_{xx}=k_1(\sqrt{F^2+x^2+y^2}-F)$ and $\varphi_{yy}=k_2(\sqrt{F^2+x^2+y^2}-F)$, GMS3 combines two focusing lenses with the same focal length F working at f_1 and f_2 under excitation of differently-polarized incident waves, respectively.

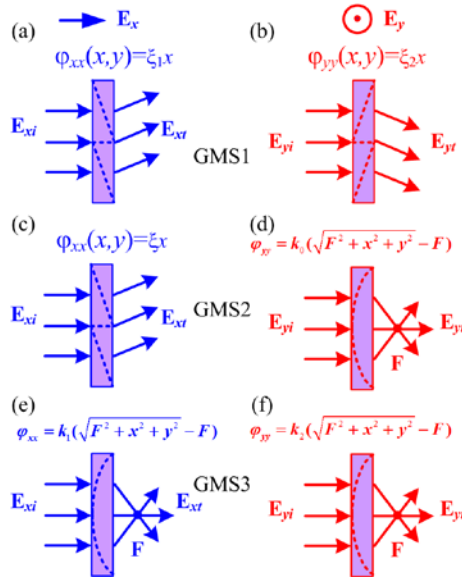


Figure 1. Schematics and working principles of the different types of transparent meta-surfaces.

GMS1 serves as a PBS with $\phi_{xx}=\xi_1 x$, $\phi_{yy}=\xi_2 x$ under excitation of (a) an x -polarized wave and (b) a y -polarized wave; GMS2 behaves as (c) a beam deflector and (d) a focusing lens with $\phi_{xx}=\xi_1 x$, $\phi_{yy} = k_2(\sqrt{F^2 + x^2 + y^2} - F)$; GMS3 operates at frequencies of (e) f_1 and (f) f_2 with $\phi_{xx} = k_1(\sqrt{F^2 + x^2 + y^2} - F)$, $\phi_{yy} = k_2(\sqrt{F^2 + x^2 + y^2} - F)$ under illuminating of different polarizations.

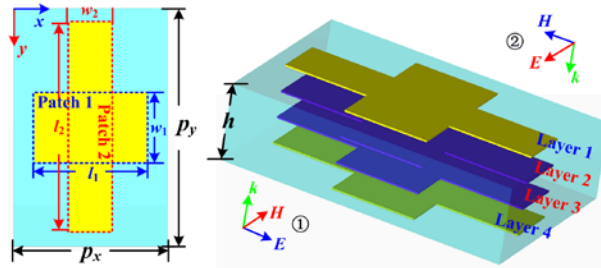


Figure 2. Topology and simulation setup of the proposed ABBA element.

(a) Top view of the basic element. The final geometrical parameters are listed as: $p_x=11$ mm, $p_y=17$ mm, $w_1=5$ mm, $w_2=4$ mm. (b) Perspective of the ABBA element and the simulation setup.

To design a high-performance transparent GMS, the first step is to find a proper element which is totally transparent but with transmission phases changeable via structural tuning. For a commonly used cascaded element, the variation in phase is typically linked with that in transmission amplitude, which generates fluctuations in the transmission spectrum. Here, we propose an ABBA system to improve the transmission amplitude by modulating the coupling among the cascaded layers, as shown in Fig. 2. In fact, the AAAA system is a special case of the ABBA system. The center frequencies for the proposed element are arranged as $f_1=6.5$ GHz and $f_2=10.5$ GHz. A basic patch structure can exhibit a perfect transmission at a particular frequency, induced by the Lorentz resonance. As seen in Fig. 2(a), a pair of orthogonal patches (patch 1 for x polarization, patch 2 for y polarization) are introduced to realize a dual-band operating property and a high isolation between different frequencies. The adopted substrate is the commonly used F4B material with $h=4.5$ mm, $\epsilon_r=2.65$, $\tan \delta=0.001$. Then, we will make a fair comparison between two typical elements, composing of a conventional AAAA system and a proposed ABBA system, respectively, with the topologies shown in the inset of Fig. 3. In this special case, the I-shaped structures change the coupling among cascaded layers, resulting in a tunable

transmission. It is worth noting that the transmission phase ϕ_{yy} is almost consistent from 4 to 8 GHz for the two elements. However, compared with AAAA element, the transmission coefficient has been significantly enhanced from 0.73 to 0.95 at the frequency of f_1 . Straightforwardly, the transmission coefficients at other transmission phases can be manipulated with the same manner. Referring to Fig. 4(a), at frequency of f_1 , within a 360° range for transmission phase, the variation of $|t_{yy}|$ is 0.73-1.0 for the conventional AAAA system, but shrinks to 0.88-1 for the proposed ABBA system. The frustrations in the transmission band have been largely suppressed. Therefore, adopting ABBA elements to design our transmissive meta-surface can surely enhance the overall working efficiencies of the device. At frequency of f_2 , see Fig. 4(b), the transmission $|t_{xx}|$ of the AAAA system keeps higher than 0.85 with a changeable l_1 , which is adopted for a design convenience. Moreover, the polarization-independent property is demonstrated by the consistent transmission phases ϕ_{xx} at f_1 and ϕ_{yy} at f_2 , which provides a high isolation between two operating frequencies and makes the 2-D wavefront control possible [9].

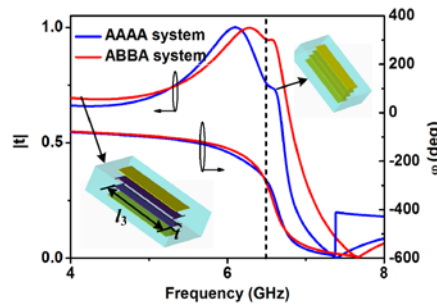


Figure 3. Transmission coefficients and transmission phases for different elements with the topology shown in the inset.

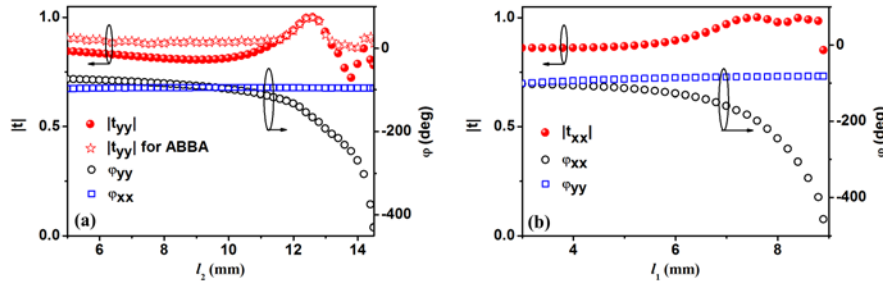


Figure 4. Final EM responses at frequencies of f_1 and f_2 under different polarizations.

- (a) Transmission coefficients and transmission phases as a function of (a) l_2 at f_1 under excitation of an x -polarized wave and (b) l_1 at f_2 under excitation of a y -polarized wave for ABBA system.

3. Numerical results of high-efficiency dual-band focusing lens

The optimized ABBA system offers us the possibility to find a unit with an arbitrary transmission phase at dual operating frequencies. Here, we design a dual-band focusing lens with the parabolic transmission phase distributions satisfying $\phi = k_i(\sqrt{F^2 + x^2 + y^2} - F)$ ($i=1, 2$), where k_i and F denotes the wave vector at frequency of f_i and the focal length, respectively. Here, $F=75$ mm is arranged for both frequencies. Fig. 5(c) plots the calculated transmission phase distributions at $f_2=10.5$ GHz (the phase distributions at $f_1=6.5$ GHz is not given for brevity). Then, the dual-band focusing lens is designed with the pictures displayed in Figs. 5(a) and 5(b). To elucidate the key point of phase compensation, the electric field of E_x at f_2 along x axis (pink lines in Figs. 5(a) and 5(b)) are displayed clearly in Fig. 5(d) and the field is normalized to the maximum case (E_y at $f_1=6.5$ GHz is not given for brevity). Here, two points should be highlighted. Firstly, high transmission is obtained for each element at both frequencies. Secondly, parabolic phase distributions are clearly demonstrated.

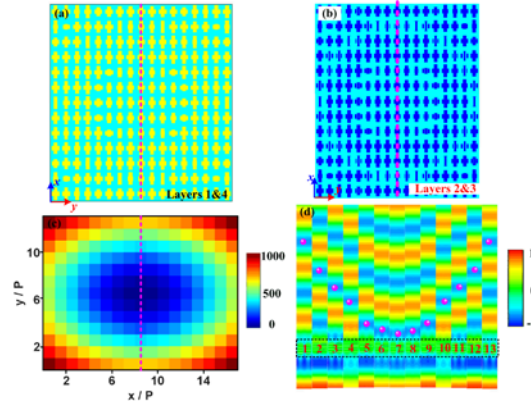


Figure 5. Design of the dual-band transparent focusing lens.

- (a) Top view of the designed dual-band focusing lens (a) in layers 1 and 4 and (b) in layers 2 and 3; (c) The required phase distribution at f_2 ; (d) FDTD simulated E_x at f_2 along the red lines in (a) and (b).

To provide a physical insight into the focusing effects at both frequencies, we evaluate the E -field based on FDTD simulations. Fig. 6(a) depicts the simulated $\text{Re}(E_y)$ distribution of a plane wave operating at f_1 , and a continuous wavefront is unambiguously observed at xoz plane. Illuminating our dual-band focusing lens with an x -polarized plane wave at frequency of f_1 , the $\text{Re}(E_y)$ distribution at xoz plane is displayed in Fig. 6(b). As expected, perfect focusing effect is observed by the largely enhanced E_y around the focal point of the meta-surface. Moreover, an almost consistent wavefront at the input part demonstrates the minimal reflection and high efficiency of the focusing lens. We can identify the focal point by evaluating the E -field intensity distribution at xoz plane, as shown in Fig. 6(c). The maximum intensity at $z=75$ mm is found to be the focal point with $F=75$ mm, which coincides well with that of the designed value ($F=75$ mm). By rotating our meta-surface with 90° , a transparent focusing lens working at f_2 is pre designed. Compared with the plane wave shown in Fig. 6(e), the designed meta-surface enables the incident uniform wavefront to be converged tightly at a focal length of $F=75$ mm, shown in Figs. 6(f) and 6(g). The simulated focal length is consistent with that of the designed value ($F=75$ mm) for a second time. The decent focusing effects come from the strong phase compensating capacity of the meta-surface and also the exact design. Fig. 6(d) compares the normalized E -field intensity along z axis between the focusing lens and the referenced plane wave at both frequencies. A simple calculation indicates that the energy at the focal point is about 20 times larger than that of the plane wave at f_2 and 16 times at f_1 . The enhanced field can also be validated by the E -field intensity along the line of $z=75$ mm, with the numerical results shown in Fig. 6(h).

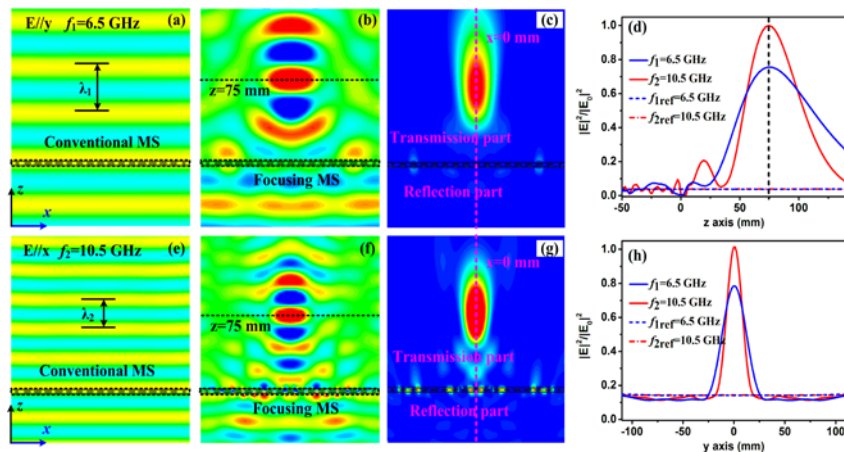


Figure 6. Focusing effects of the dual-band transparent lens.

E -field distributions of the referenced plane waves at (a) f_1 and (e) f_2 and of proposed dual-band focusing lens at (b) f_1 and (f) f_2 ; The power distributions for (c) f_1 and (g) f_2 ; Comparison of normalized E -field intensity along (d) z axis and (h) $z=75$ mm.

4. Dual-band lens antenna (LA) with improved radiation characteristics

Here, we try to improve the radiation characteristics of the dual-band LA by employing ABBA-designed focusing lens, which largely enhances the system transmission. The topology of the proposed dual-band LA is displayed in Fig. 7(a). Self-made Vivaldi antenna, operating in a wide bandwidth from 4 to 12 GHz, is applied as the feed antenna, which can generate quasi-spherical waves at both frequencies of f_1 and f_2 . The parameter $l=71$ mm is optimized to obtain best radiation patterns at both frequencies. Then, we fabricate the focusing lens and the Vivaldi antenna with a standard printed-circuit-board (PCB) technology, with the pictures shown in Fig. 7(c).

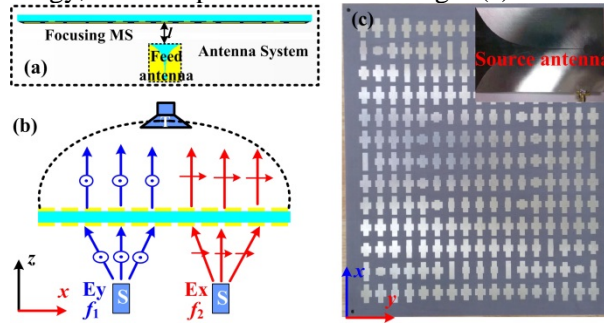


Figure 7. The (a) simulation model, (b) measurement schematic, and (c) the fabricated pictures for the dual-band LA.

For experimental demonstration, we measure the 2-D radiation patterns of the LA in two principal radiation planes through a far-field measurement system in an anechoic chamber. As seen in Fig. 8, the simulated and measured results are in reasonably consistent in all cases. Under excitation of a y-polarized wave at frequency of f_1 , the measured (simulated) half power beam width (HPBW) is about 126.5° (127.3°) in E plane (xoz plane) and 91.2° (91.5°) in H plane ($yo z$) for the Vivaldi antenna, respectively. However, the HPBW reduces significantly to 13.5° (13.4°) and 14° (14.2°) in above mentioned planes for the LA, respectively. The measured (simulated) gain is about 18.7 dB (18.7 dB) for the LA, and a simple calculation shows that the gain has increased about 13.1 dB (13.2 dB) compared with that of the bare Vivaldi antenna. At frequency of f_2 , the measured (simulated) HPBW is about 10.2° (10.4°) at E plane ($yo z$ plane), 9.3° (9.4°) at H plane (xoz plane), respectively. A significant beam-width reduction of about 72.5° (68.8°) at E plane, 44.3° (42.5°) at H plane is achieved for the LA at f_2 . The measured (simulated) radiation gain is about 23 dB (23.2 dB), 9.2 dB (9.4 dB) for the TA and bare Vivaldi antenna, respectively. Note that the aperture efficiency is evaluated with respect to the utmost directivity which can be calculated through the equation $\eta = G/D_{\max} = G/(4\pi PQ/\lambda_0^2) \times 100\%$. The aperture efficiency of 30.3% (30.3%) is obtained at f_1 , and 31.3% (32.8%) at f_2 , respectively. Further analysis indicates that the F/B ratio is better than 15.5 dB in all cases. The side-lobe levels for all numerical results (experimental results) are about 16.3 dB (15.4 dB) lower than those of the mainlobe. The 1 dB gain bandwidth is evaluated as about 0.7 GHz (6.1-7 GHz), 1.2 GHz (9.8-11 GHz) at f_1 and f_2 , respectively.

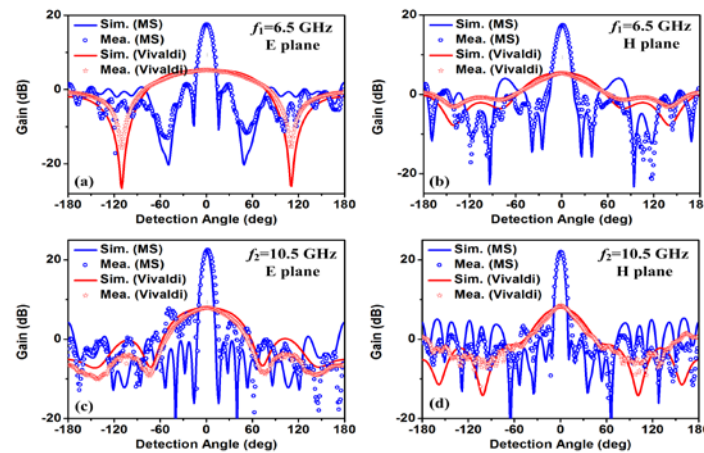


Figure 8. Simulated and measured radiation patterns at f_1 (a) xoz plane; (b) $yo z$ plane and at f_2 (a) $yo z$ plane; (b) xoz plane.

5. Conclusion

A novel LA operating in both C and X bands with improved radiation characteristics has been numerically and experimentally demonstrated by employing a high-performance transparent meta-surface. The designed LA shows a series of advantages such as high radiation gain of 18.7 dB at f_1 and 23 dB at f_2 , competitive aperture efficiencies better than 30% at both frequencies and comparable wide bandwidth. Our numerical and experimental results can stimulate the realizations of high-performance transparent meta-surfaces working in other frequencies or achieving other integrated functionalities.

References

- [1] Yu N, Genevet P and Kats M A 2011 Light propagation with phase discontinuities: generalized laws of reflection and refraction *Science* **334** 333-338
- [2] Huang L, Chen X, Mühlenbernd H and Zhang H 2013 Three-dimensional optical holography using a plasmonic metasurface *Nat. Commun.* **4** 2808
- [3] Ma H F, Wang G Z and Kong G S 2015 Independent controls of differently-polarized reflected waves by anisotropic metasurfaces *Sci. Rep.* **5** 9605
- [4] Khorasaninejad M, Chen W T and Devlin R C 2016 Metalenses at visible wavelengths: diffraction-limited focusing and subwavelength resolution imaging *Science* **352** 1190
- [5] Wan X, Shen X, Luo Y and Cui T J 2014 Planar bifunctional Luneburg-fisheye lens made of an anisotropic metasurface *Laser Photonics Rev.* **8**(5) 757-765
- [6] Li H, Yuan L H and Zhou B Ultrathin multiband gigahertz metamaterial absorbers 2011 *J. Appl. Phys.* **110** 014909
- [7] Shen X, Cui T J and Zhao J 2011 Polarization-independent wide-angle triple-band metamaterial absorber *Opt. Express* **19**(10) 9401-9407
- [8] Huang C, Pan W, Ma X and Luo X 2016 Multi-spectral metasurface for different functional control of reflection waves *Sci. Rep.* **6** 23291
- [9] Cai T, Wang G M and Zhang F X 2015 Ultra-thin polarization beam splitter using 2-D transmissive phase gradient metasurface *IEEE Trans. Antennas Propag.* **63**(12) 5629-5636
- [10] Sun W, He Q, Sun S and Zhou L 2016 High-efficiency surface plasmon meta-couplers: concept and microwave-regime realizations *Light: Sci. Appl.* **5** e16003
- [11] Pfeiffer C and Grbic A 2013 Metamaterial Huygens' surfaces: tailoring wave fronts with reflectionless sheets *Phys. Rev. Lett.* **110** 197401